RSC Advances

PAPER

View Article Online
View Journal | View Issue

Cite this: *RSC Adv.*, 2025, **15**, 35219

Carboxymethylcellulose functionalized magnetic graphene oxide for the efficient removal of tetracycline from aqueous media

Nosheen Tabassum Dipannita,[b] Sabina Yasmin, *[c] Md. Kamrul Hasan,[b] Md. Sanwar Hossain,[c] Monira Akter Somapti [b] and Md Humayun Kabir *[a]

A carboxymethylcellulose (CMC) functionalized magnetic graphene oxide (m-GO/Fe_3O_4/CMC) nanoadsorbent was successfully synthesized to remove tetracycline (TC) in aqueous media. The prepared m-GO/Fe_3O_4/CMC nanoadsorbent was characterized using several instrumental techniques, including X-ray diffractometry, Fourier transform infrared spectroscopy, vibrating sample magnetometry, point of zero charge, transmission electron microscopy, scanning electron microscopy, and energy dispersive-X-ray. These techniques confirmed the successful synthesis of this nanoparticle and also revealed its superparamagnetic behavior, exhibiting a saturation magnetization of 50.69 emu g^{-1}. The batch adsorption experiments were carried out under varying conditions, including adsorbent dosage, contact time, pH, initial concentration, and temperature, to determine the optimum conditions for the adsorption process. A maximum removal efficiency of 96.04% was achieved within just 25 min using a dosage of 0.1 g L^{-1} at pH 5. Kinetic analysis revealed that the adsorption followed the pseudo-second-order model, indicating that the uptake of TC was primarily governed by chemisorption. This behavior could be attributed to hydrogen bonding, electrostatic interactions, and π–π stacking between the adsorbate and the adsorbent. The isotherm data were best described by the Langmuir isotherm, with a maximum adsorption capacity of 54.73 mg g^{-1}, suggesting monolayer adsorption dominated by electrostatic interactions on heterogeneous surface sites. Furthermore, reusability tests revealed the nanoadsorbent's excellent stability, retaining high adsorption efficiency even after ten consecutive cycles. The findings unambiguously demonstrated that this m-GO/Fe_3O_4/CMC nanoadsorbent could be a good choice to remove TC from wastewater sources.

Received 3rd September 2025
Accepted 16th September 2025

DOI: 10.1039/d5ra06621b

rsc.li/rsc-advances

1. Introduction

In modern health care, antibiotics are crucial for treating bacterial infections.[1] These medications, which either kill bacteria or inhibit their growth, have been widely used and have had a profound impact on medical advancements.[2] Tetracycline (TC) is a widely used antibiotic due to its strong antibacterial properties.[3] However, it undergoes only partial metabolism in humans and animals, with a significant portion being excreted through urine and feces.[4] As a result, TC residues persist in the environment, particularly in agricultural runoff and municipal wastewater.[5] However, due to its limited metabolism, significant amounts of TC are released into the environment, raising concerns related to its impact on human health and ecosystems.[6] Alarming levels of residual antibiotics have been detected in both groundwater and surface water.[7] Even low levels of TC exposure can disrupt aquatic microorganisms, hinder the spread of beneficial bacteria that combat antibiotic resistance, and contribute to increasing antibiotic resistance.[5] Consequently, removing TC from contaminated environments is essential to protect both ecosystems and public health.[8]

Various methods are accessible for removing antibiotics from aqueous media, including adsorption,[9] biodegradation,[10] advanced oxidation processes,[11] photocatalysis,[12] membrane technology,[13–15] and photodegradation.[16] Among these, adsorption stands out as the most economical and environmentally friendly alternative.[17] It is easy to handle and highly efficient, it produces negligible byproducts, and it can be effortlessly scaled up.[18] In spite of its advantages, adsorption has certain limitations, such as lengthy processing times, high dosage requirements, and challenges in separating the adsorbent.[19] These issues can be addressed by the functionalization and optimizing performance of the adsorbent, enabling TC removal at lower doses and in shorter times. Thus, developing a cost-

[a]*Institute of Food Science and Technology (IFST), Bangladesh Council of Scientific and Industrial Research (BCSIR), Dhanmondi, Dhaka-1205, Bangladesh. E-mail: humayunkabir@bcsir.gov.bd*

[b]*Department of Chemistry, University of Dhaka, Dhaka-1000, Bangladesh*

[c]*Institute of National Analytical Research and Service (INARS), Bangladesh Council of Scientific and Industrial Research (BCSIR), Dhanmondi, Dhaka-1205, Bangladesh. E-mail: sabinayasmin@bcsir.gov.bd*

effective and highly efficient removal method is essential.[17] Various adsorbents, such as activated carbon,[20] multi-walled carbon nanotubes,[21–23] sludge biochar,[24] and goethite[4] have been developed and utilized to remove TC from environmental samples. However, these methods still face inherent limitations, including low adsorption capacity, slow adsorption rates, and limited reusability.[17]

Graphene oxide (GO) based composites have recently gained significant attention as effective adsorbents for removing diverse pollutants.[25] Their application in wastewater treatment offers remarkable advantages.[26] Owing to their unique characteristics, such as a large specific surface area, abundant surface functional groups, π-electron-rich planar structure, superior mechanical and chemical stability, excellent electrical and thermal conductivity, high optical transparency, low density, and strong compatibility with other materials, GO stands out as a highly efficient adsorbent.[27–29] The high cost and limited global availability of pure graphite and GO pose challenges.[30] This issue can be addressed by synthesizing GO from electronic waste, particularly waste Li-ion batteries.[31] These batteries, widely discarded by the electronics industry, cause environmental hazards due to toxic leaching.[32] Their graphite electrodes offer a sustainable source for GO production, simultaneously providing raw materials and promoting waste management.[33] Besides, GO serves as an excellent precursor for such materials due to its abundance of hydrophilic functional groups, including epoxide, carbonyl, carboxyl, and hydroxyl groups, which are distributed across both its edges and basal plane.[34] These functional groups facilitate strong interactions with other hydrophilic agents through hydrogen bonding, π–π interactions, and electrostatic forces.[35] Among these agents, carboxymethylcellulose (CMC), a water-soluble derivative of cellulose, is often preferred due to its natural abundance, biocompatibility, and eco-friendly nature. Its diverse functional properties, including high water solubility and abundant oxygen-containing groups, make it an amazing structure that significantly enhances the efficiency of antibiotic removal, supporting a comprehensive and sustainable strategy for mitigating the environmental impact of antibiotics.[36]

Conversely, GO-based adsorbent materials exhibit good dispersion in water due to their nanoscale particle size and the abundance of hydrophilic functional groups on their surface.[37] Consequently, despite the high adsorption efficiency of GO and GO-based nanoadsorbents, a significant challenge remains in their separation from the treated solution after the adsorption process.[38] To overcome this limitation, the integration of magnetic nanomaterials is essential.[39] By incorporating magnetic nanoparticles, GO-based nanoadsorbents can be easily separated, offering a more effective and practical solution for wastewater treatment.[40] Moreover, a complex sorbent based on graphene and CMC not only enhances adsorption efficiency but also imparts mechanical flexibility, chemical stability, and reusability to the sorbent. These features enable the adsorption of a wide range of pollutants while permitting the flexible integration of various components to develop multifunctional highly efficient, recyclable, and eco-friendly materials tailored for specific applications.[41]

To the best of our knowledge, no research has been reported on the application of m-GO/Fe_3O_4/CMC nanoadsorbents for the removal of TC from aqueous solutions. In this study, a magnetically separable m-GO/Fe_3O_4/CMC nanocomposite was synthesized utilizing electronic waste by incorporating magnetic Fe_3O_4 and CMC with GO. The structural and chemical properties of the nanocomposite were comprehensively characterized by using various analytical techniques. The synthesized magnetic material was then applied for the adsorption of TC from aqueous solutions. The adsorption performance was systematically evaluated under different conditions, including adsorbent dose, contact time, solution pH, initial TC concentration, and temperature. Furthermore, the adsorption mechanism was investigated through kinetic and isotherm analyses. The reusability of the prepared adsorbent for TC removal was also assessed to determine its potential for practical applications.

2. Materials and method

2.1 Reagents and chemicals

TC (Purity ≥95%, CAS No: 64-75-5) was obtained from Sigma-Aldrich, and its physical and chemical characteristics are summarized in Table 1. Iron(II) sulfate heptahydrate ($FeSO_4 \cdot 7H_2O$) (ACS reagent, 99%, CAS: 10025-77-1) and iron(III) sulfate heptahydrate ($Fe_2(SO_4)_3 \cdot 7H_2O$) (99%, CAS: 13478-10-9) were purchased in Sigma Aldrich from Switzerland. CMC (Purity ≥99.5, CAS No: 9004-32-4) was obtained from BDH Chemicals Ltd, Poole, England. Formic acid (FA) and LC-MS/MS grade acetonitrile (ACN) were purchased from AppliChem GmbH, Ottoweg, D-64291 Darmstadt, Germany. Sulfuric acid (H_2SO_4) (95–97%, CAS: 7664-93-9) and potassium permanganate ($KMnO_4$) (≥99.0%, CAS: 7722-64-7) were sourced from Sigma-Aldrich, USA. Phosphoric acid (H_3PO_4) (85%, CAS: 7664-38-2) was acquired from JANSSEN CHEMICA, Belgium, while hydrochloric acid (HCl) (37%, CAS: 7647-01-0) and ethanol (C_2H_5OH) (98%, CAS: 64-17-5) were purchased from AppliChem, Germany. Sodium hydroxide (NaOH) (Purity ≥98%, CAS No: 1310-73-2), potassium chloride (KCl) (Purity ≥99%, CAS No: 7447-40-7) and hydrogen peroxide (H_2O_2) (30%, CAS: 7722-84-1) were also collected from Sigma-Aldrich, USA. Throughout the experiments, deionized (DI) water with a resistivity of 18 MΩ cm was used to prepare all solutions.

2.2 Instrumentation

For the analysis of TC samples, an Agilent 1290 Infinity II LC module was used in conjunction with a 6420 LC/TQ triple quadrupole mass spectrometer. Analytical separation was performed using a ZORBAX RRHD Eclipse Plus C18 column (2.1 × 100 mm, 1.8 μm particle size). The binary mobile phase consisted of 0.1% formic acid (FA) in water (A) and acetonitrile (B), with a constant flow rate of 0.35 mL min^{-1}. A linear isocratic mobile phase was employed, comprising 50% A and 50% B. The analyte was analyzed using positive electron spray ionization (ESI+) in liquid chromatography-tandem mass spectrometry (LC-MS/MS). Multiple reaction monitoring (MRM) mode was

Table 1 Physical and chemical characteristics of TC

Formula	$C_{22}H_{24}N_2O_8$
Molar mass (g mol^{-1})	444.4
Water solubility (mg L^{-1})	231
Polar surface area	181.62 Å^2
Number of rings	4
Melting point	172.5 °C
Molecular structure	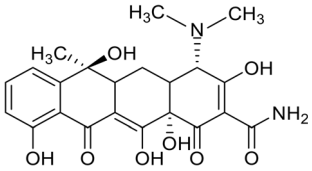

utilized with a transition from the precursor ion ($M + H^+$) 445.1 to the product ions 427.4 and 410.2, applying collision energies (CE) of 15 and 20 eV, respectively. Both transitions had a dwell voltage of 110 V. Fourier transform infrared (FTIR) spectra were obtained using a SHIMADZU IRPrestige-21 spectrometer (Japan). Surface morphology and elemental composition of m-GO/Fe_3O_4/CMC were analyzed using transmission electron microscopy (TEM) (model: Talos $F_{200}X$ G_2, Thermo Fisher Scientific, USA, operating at 200 kV) and scanning electron microscopy (SEM) (EVO18, Carl Zeiss AG, Germany) at various magnifications with a 15 kV electron beam voltage with energy dispersive X-ray spectroscopy (EDS) (TEAM EDS; EDAX, USA). X-ray diffraction (XRD) patterns were measured with a diffractometer (Rigaku Ultima IV, Japan) equipped with a Cu Kα source (λ = 1.541 Å). The magnetic characterization of the prepared m-GO/Fe_3O_4/CMC nanocomposite was performed using a vibrating sample magnetometer (VSM) within the Physical Property Measurement System (PPMS, Quantum, US) at 300 K.

2.3 Collection of graphite powder

Graphite powder was recovered from abandoned Li-ion batteries collected from residential areas. The adherent paste of Li-ion batteries was composed of MnO_2, NH_4Cl, carbon powder, graphite rods and other materials. The Li-ion batteries were carefully dismantled to extract graphite rods. Then the rods were rinsed thoroughly with DI water and blotted with filter paper to remove any residual paste, NH_4Cl, carbon powder and other contaminants. Upon drying in air, the graphite rods were crushed into a fine powder using a mortar and pestle. The resulting graphite powder was treated with Aqua Regia and thoroughly washed with DI water to eliminate unwanted inorganic contaminants. Finally, it was dried at 60 °C for 24 hours.[33,42]

2.4 Synthesis of GO

Graphene oxide (GO) was synthesized from recovered graphite powder obtained from waste Li-ion batteries using the modified Hummers' method.[28,43,44] Briefly, 270 mL of H_2SO_4 and 30 mL of H_3PO_4 were mixed in a round-bottom flask and stirred for 10 min. Then, 2 g of graphite powder was gradually added to the solution, followed by 12 g of $KMnO_4$. The mixture was heated to 50 °C and maintained at that temperature for 12 hours. Once the solution turned deep green, it was allowed to cool to room temperature before being placed in an ice bath. Subsequently, 6 mL of 30% H_2O_2 was added to eliminate excess $KMnO_4$. Due to the exothermic nature of this reaction, the temperature was kept close to 0 °C using an ice bath. The mixture was then centrifuged at 6000 rpm, and the resulting solid was washed sequentially with DI water and 30% HCl to remove metallic impurities, followed by additional washing with DI water to reduce chloride content, and finally with ethanol. Finally, the synthesized GO was then dried in a vacuum drying oven at 50 °C for 24 hours.

2.5 Synthesis of m-GO/Fe_3O_4/CMC

A total of 80 mg of GO was dispersed in 50 mL of DI water and sonicated for 30 min. Simultaneously, 0.01 mol of $FeSO_4 \cdot 7H_2O$ (2.781 g) and 0.02 mol of $Fe_2(SO_4)_3 \cdot 7H_2O$ (7.998 g) were dissolved in 100 mL of deionized water and sonicated for 30 min at ambient temperature. Separately, 80 mg of CMC was dissolved in 50 mL of deionized water. The GO suspension (50 mL) and CMC solution (50 mL) were then combined in a round-bottom flask and heated in an oil bath. The ferric–ferrous ion solution was gradually added to this mixture, which was stirred continuously for 30 min at 45 °C. A 2.0 M NaOH solution was slowly introduced as a precipitating agent until the pH reached approximately 11. The mixture was then heated at 85 °C under continuous stirring for 2 hours before being cooled to room temperature. The obtained precipitate was isolated with the aid of an external magnetic field and rinsed with DI water repeatedly until the pH reached neutrality, followed by ethanol washing. Finally, the black precipitate was dried in a vacuum drying oven at 60 °C for 18 hours and designated as the m-GO/Fe_3O_4/CMC nanoadsorbent (Scheme 1).

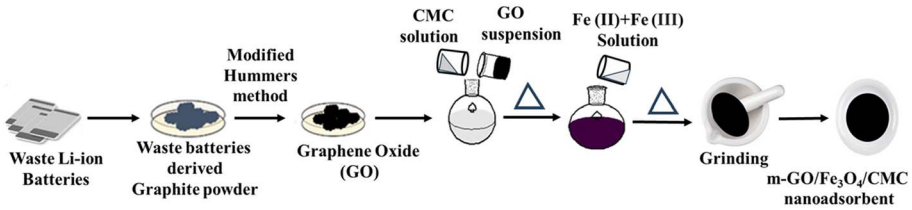

Scheme 1 Schematic of m-GO/Fe_3O_4/CMC nanoadsorbent synthesis.

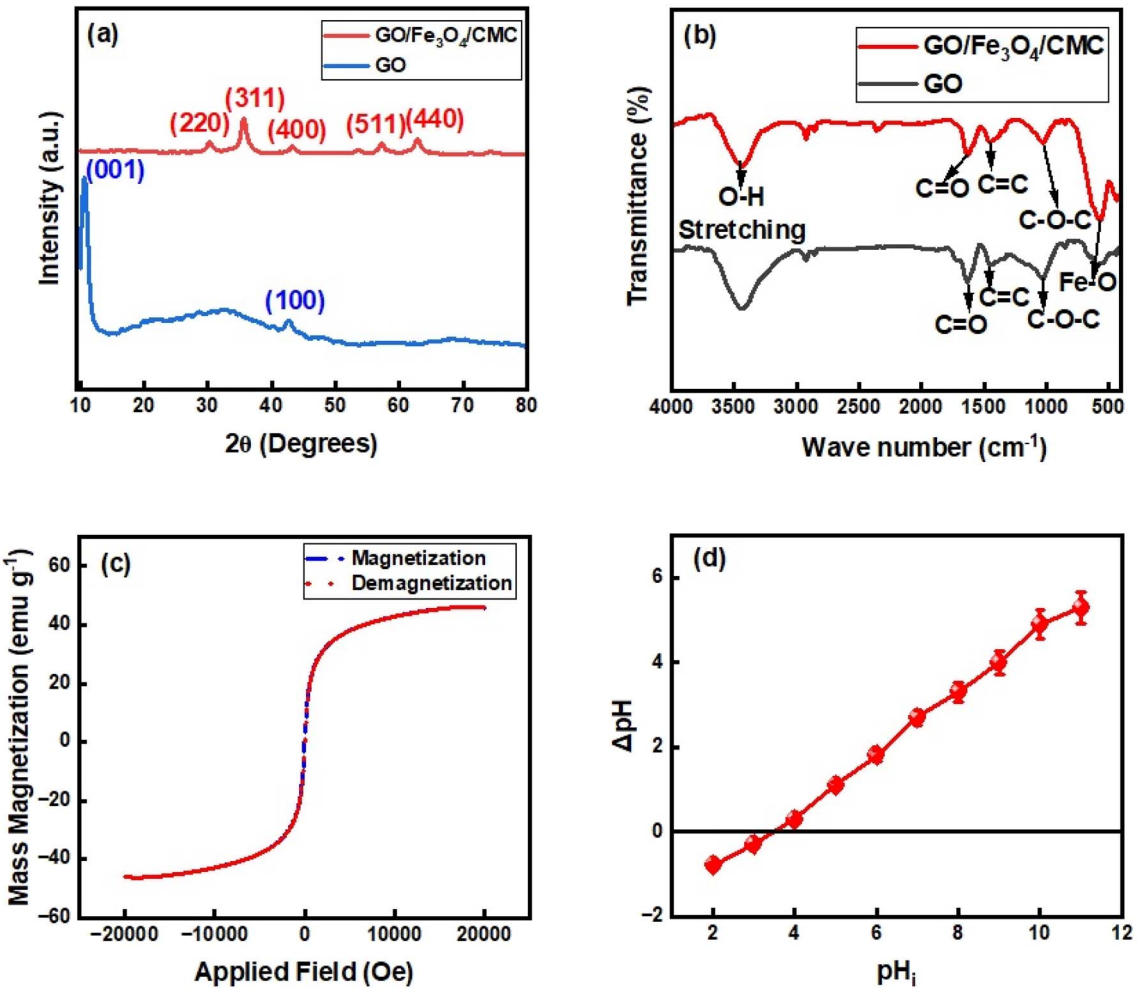

Fig. 1 (a) XRD pattern of GO and m-GO/Fe_3O_4/CMC, (b) FTIR spectra of GO and m-GO/Fe_3O_4/CMC, (c) magnetization curve of m-GO/Fe_3O_4/CMC and (d) point of zero charge of m-GO/Fe_3O_4/CMC.

2.6 Batch adsorption studies

In each batch experiment, each trial was performed in 100 mL conical flasks. For the batch adsorption experiments, the sample flasks were wrapped in aluminum foil to prevent any degradation or additional adsorption. A stock solution of TC (100 mg L^{-1}) was diluted with DI water to prepare various TC solutions with different initial concentrations. Different amounts of the nanoadsorbent (1–10 mg) were added to 20 mL of TC solution. Before adding the adsorbent, the pH of the mixture was adjusted to the desired level using 0.1 M HCl or NaOH solutions. The flasks were then stirred at 250 rpm for a specific period to allow the system to reach equilibrium. After stirring, the solutions were filtered using CHROMAFIL® Xtra syringe filters with a pore size of 0.22 μm before measuring the concentrations. The effects of contact time (5–90 min), solution pH (2.0–10.0), and initial concentration (0.2–10.0 mg L^{-1}) of TC were investigated to determine the optimal conditions for the adsorption process. The experiments were designed by varying one parameter at a time while keeping the others constant. A kinetic study and isothermal analysis were also conducted. In the kinetic study, the contact time was varied from 5 to 90 min, while in the isothermal study, the initial concentration ranged from 0.2 to 10 mg L^{-1}, with the temperature varying between 25 °C and 50 °C. To evaluate the concentration of TC before and after adsorption, liquid chromatography-tandem mass spectrometry (LC-MS/MS) was employed. The removal percentage of the TC antibiotic was calculated using eqn (1):[45]

$$\text{Removal percentage} = \frac{C_o - C_t}{C_o} \times 100\% \quad (1)$$

where C_o and C_t were the initial and at time t concentration of TC (mg L^{-1}) respectively.

The adsorbed amount at time t (q_t) and at equilibrium (q_e) were calculated by using eqn (2) and (3) (ref. 46), where q_t, q_e were the amount of TC adsorbed at time t and at equilibrium per unit mass of adsorbent (mg g^{-1}); C_t and C_e were the concentrations (mg L^{-1}), at time t and at equilibrium, respectively.

$$q_t = \frac{C_o - C_t}{M} \times V \quad (2)$$

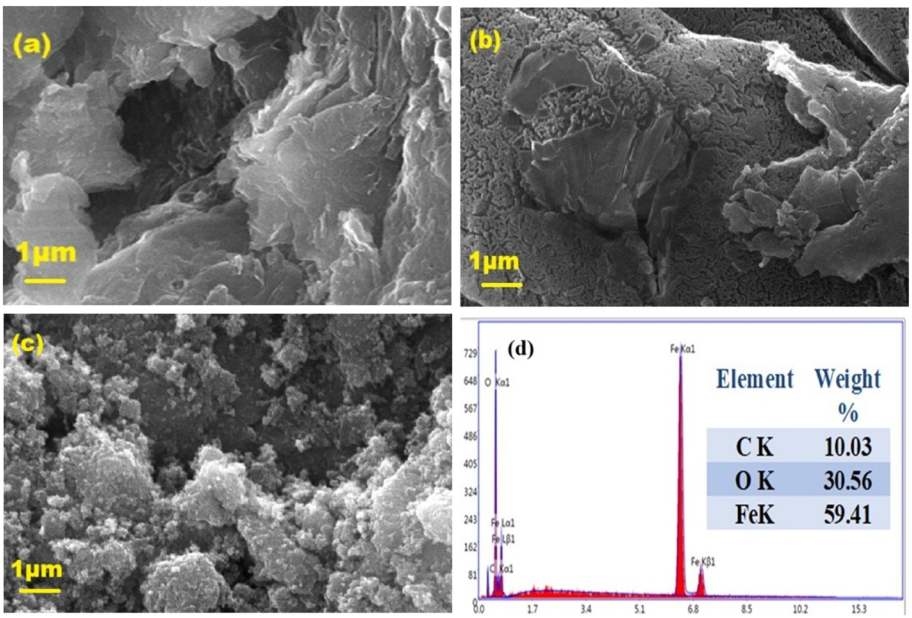

Fig. 2 SEM images of (a) GO, (b) CMC, (c) m-GO/Fe_3O_4/CMC and (d) EDX spectra of m-GO/Fe_3O_4/CMC.

$$q_e = \frac{C_o - C_e}{M} \times V \quad (3)$$

V was the solution volume taken for batch experiments in liter (L), and M was the mass of adsorbent in gram (g).

3. Results and discussion

3.1 Characterization of m-GO/Fe_3O_4/CMC

3.1.1. X-ray diffraction (XRD). The X-ray diffraction (XRD) patterns of synthesized GO and the m-GO/Fe_3O_4/CMC nanocomposite are presented in Fig. 1(a). The XRD pattern of GO exhibited a characteristic peak at $2\theta = 10.66°$, corresponding to the (001) plane with an interlayer spacing of 0.83 nm. An additional peak at $2\theta = 42.61°$ was attributed to the (100) plane with an interlayer spacing of 0.21 nm, confirming the successful preparation of GO, as calculated from Bragg's law.[27,47] These findings indicate complete oxidation of graphite, with the presence of oxygen-containing functional groups on the GO surface.[47–49] In contrast, the XRD pattern of the m-GO/Fe_3O_4/CMC nanocomposite displayed five distinct peaks at 2θ = 30.15°, 35.65°, 43.11°, 57.35°, and 62.76°, corresponding to the (220), (311), (400), (511), and (440) planes, respectively. The calculated interlayer spacings for these peaks were 0.30, 0.25, 0.21, 0.16, and 0.15 nm. Notably, the sharp peak at $2\theta = 35.65°$ assigned to the (311) plane revealed an interlayer spacing of 0.25 nm, significantly smaller than the 0.83 nm spacing observed in pure GO. This reduction in interlayer spacing suggested structural modifications in the GO layers, likely due to interactions with Fe_3O_4/CMC nanoparticles, which might induce compression or rearrangement of the interlayer structure.[3] Furthermore, the reduced peak intensities in the m-GO/Fe_3O_4/CMC nanocomposite indicated smaller particle sizes, further supported the altered chemical composition compared to pure GO.[50] These results collectively confirmed the successful formation of a distinct m-GO/Fe_3O_4/CMC nanocomposite with modified structural properties.

3.1.2. Fourier transform infrared (FTIR) spectroscopy. The Fourier transform infrared (FTIR) spectra of GO and m-GO/Fe_3O_4/CMC are presented in Fig. 1(b). The GO spectrum exhibited characteristic absorption bands at 3441 cm^{-1} (O–H

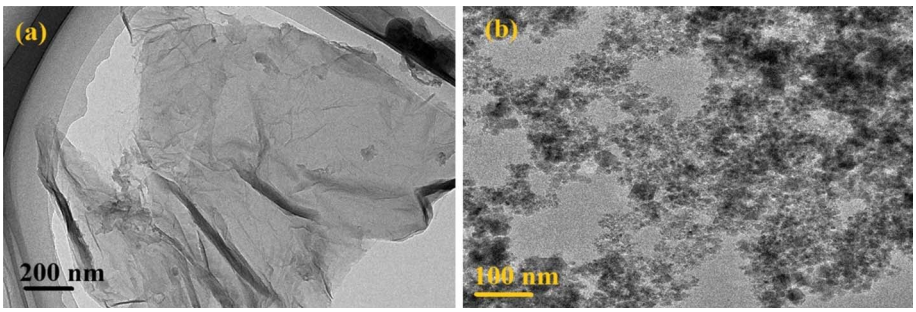

Fig. 3 TEM images of (a) GO at 200 nm and (b) m-GO/Fe_3O_4/CMC at 100 nm.

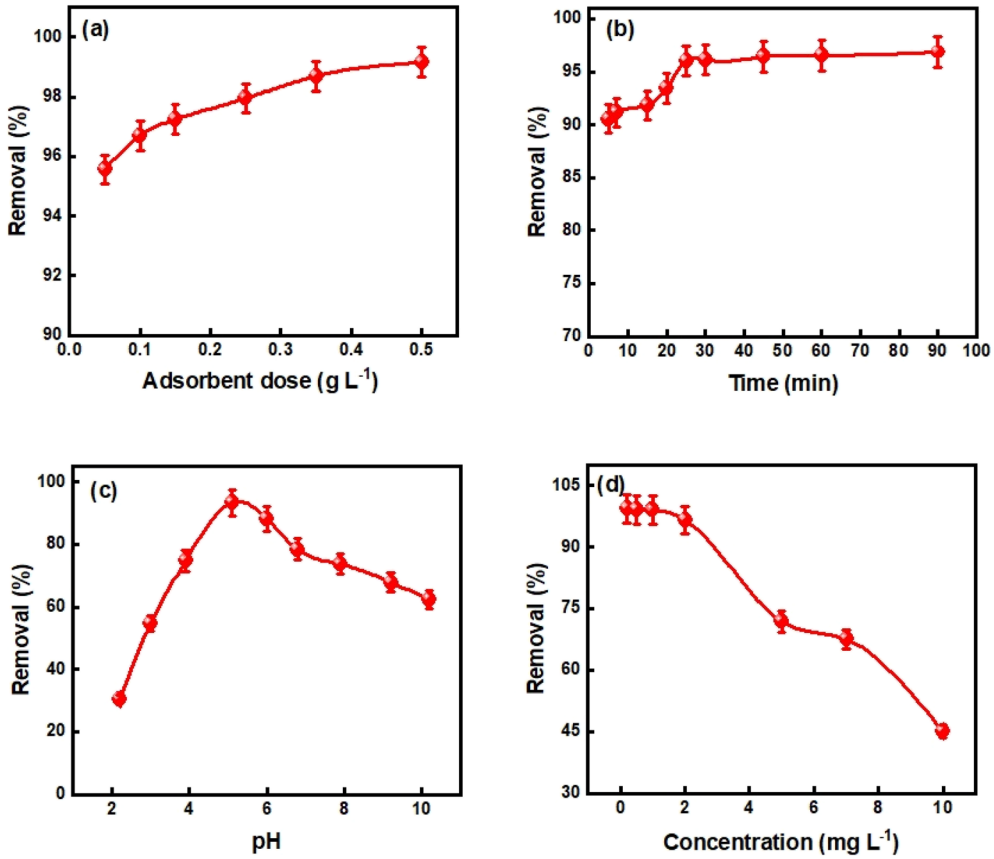

Fig. 4 Effect of (a) dose, (b) contact time, (c) pH and (d) initial concentration on TC removal by m-GO/Fe_3O_4/CMC (C_o = 2 mg L^{-1}, dose = 0.1 g L^{-1}, pH = 5, shaking speed = 250 rpm, T = 25 °C).

stretching), 1722 cm^{-1} (C=O stretching of carboxyl groups), 1442 cm^{-1} (aromatic C=C stretching), and 1030 cm^{-1} (C–O–C stretching of epoxy groups).[49,51] In contrast, the m-GO/Fe_3O_4/CMC spectrum showed significant changes. The C=O stretching vibration of carboxyl groups weakened and shifted to 1631 cm^{-1}, while the aromatic C=C and epoxy C–O–C peaks intensified and shifted to higher wavenumbers at 1454 cm^{-1} and 1157 cm^{-1}, respectively. These shifts suggested strong interactions between Fe_3O_4/CMC nanoparticles and the functional groups of GO. Additionally, a new peak appeared at 2924 cm^{-1}, corresponding to the C–H stretching vibration of the CH_2 group in CMC.[52] Further evidence of Fe_3O_4 incorporation was observed at 434 cm^{-1}, attributed to the Fe–O stretching vibration.[53] This confirmed the successful anchoring of Fe_3O_4 nanoparticles onto the GO surface. The presence of these distinct peaks in the composite spectrum verified the formation of m-GO/Fe_3O_4/CMC.

3.1.3. Vibrating sample magnetometry (VSM). The magnetic properties of the synthesized m-GO/Fe_3O_4/CMC nanocomposite were analyzed using a vibrating sample magnetometer (VSM), as shown in Fig. 1(c). The hysteresis loop, which was obtained during the magnetization and demagnetization process, revealed a magnetic saturation value of 50.69 emu g^{-1}, indicating the maximum magnetization achievable by the nanocomposite under an applied magnetic field.[54] Beyond which no further magnetization occurred.[47] The low values of remanence and coercivity observed in the hysteresis curve confirmed the superparamagnetic nature of the material, demonstrating its lack of permanent magnetization.[17] Yet, its magnetic response was still strong enough for nanoparticle separation.[55]

3.1.4. Point of zero charge (pH_{pzc}) determination. The point of zero charge (pH_{pzc}) of the m-GO/Fe_3O_4/CMC nanocomposite was determined using the solid addition method.[56] A set of flasks was prepared, each containing 50 mL of 0.01 M KCl solution, and the initial pH (pH_i) was adjusted between 2.0 and 11.0 using 0.1 M HCl or 0.1 M NaOH. Subsequently, 5 mg of the nanocomposite was added to each flask, followed by shaking at 250 rpm for 25 min to attain equilibrium. The equilibrium pH (pH_e) was then measured, and the difference between the final and initial pH values ($\Delta pH = pH_e - pH_i$) was calculated. A plot of ΔpH *versus* pH_i was constructed, and the pH_{pzc} was identified as the pH at which the curve intersected the line $\Delta pH = 0$, found to be 3.5 (Fig. 1(d)). This indicated that the surface of m-GO/Fe_3O_4/CMC was positively charged at pH values below 3.5 and negatively charged above this value.

3.1.5. Scanning electron microscopy (SEM). The representative SEM images of GO, CMC and m-GO/Fe_3O_4/CMC are shown in Fig. 2(a–c). The SEM image in Fig. 2(a) displayed the layered structure of graphene oxide characterized by a wrinkled

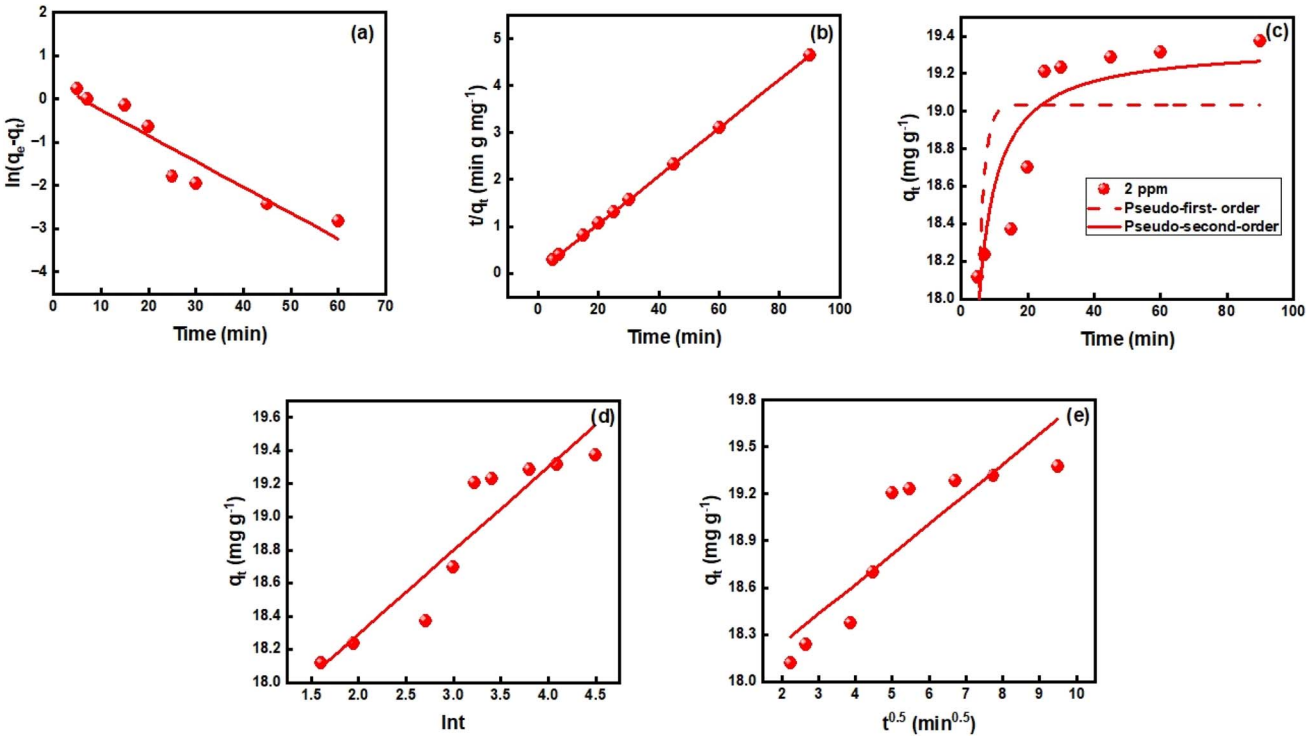

Fig. 5 (a) Linear pseudo-first-order kinetics model, (b) linear pseudo-second-order kinetics model, (c) non-linear pseudo-first-order and pseudo-second-order kinetics model, (d) Elovich kinetic model and (e) Weber–Morris intraparticle diffusion model for TC ($C_o = 2$ mg L^{-1}, pH = 5, m-GO/Fe_3O_4/CMC = 0.1 g L^{-1}, shaking speed = 250 rpm, temp = 25 °C).

surface, which likely arose from the introduction of oxygen-containing functional groups during the oxidation process.[31] These functional groups induced structural defects, resulting in a non-planar and undulating morphology.[57] The SEM image of CMC revealed a relatively smooth and irregularly layered surface morphology. The structure appeared to be amorphous and flaky, with uneven surfaces and loosely packed features. The observed morphology indicated low porosity and a compact, non-uniform texture, which was characteristic of polymeric materials like CMC.[58] The SEM image of m-GO/Fe_3O_4/CMC revealed a heterogeneous and rough surface texture, indicating the successful integration of Fe_3O_4 nanoparticles and CMC onto the graphene oxide sheets. The skeletal structure of CMC appeared to intertwine with the wrinkled morphology of GO, providing structural reinforcement and enhancing the dispersion and stabilization of magnetic Fe_3O_4 nanoparticles

Table 2 Different kinetic parameters of TC adsorption onto m-GO/Fe_3O_4/CMC

Kinetic models	Curve fitting	Parameters	TC
Pseudo-first-order	Linear	q_e (mg g^{-1})	1.4174
		k_1 (g mg^{-1} min^{-1})	0.0597
		R^2	0.8895
Pseudo-second-order	Linear	q_e (mg g^{-1})	19.5008
		k_2 (g mg^{-1} min^{-1})	0.0900
		R^2	0.9999
Non-linear pseudo-first-order	Non-linear	q_e (mg g^{-1})	19.0358
		k_1 (g mg^{-1} min^{-1})	0.5658
		R^2	0.4777
Non-linear pseudo-second-order	Non-linear	q_e (mg g^{-1})	19.3522
		k_2 (g mg^{-1} min^{-1})	0.1282
		R^2	0.8004
Elovich model	Linear	α (mg g^{-1} min^{-1})	3.8090×10^{14}
		β (g mg^{-1})	1.9819
		R^2	0.8711
Weber–Morris intraparticle diffusion model	Linear	K_i (mg g^{-1} $min^{-0.5}$)	0.1920
		C_i (mg g^{-1})	17.8541
		R^2	0.7783

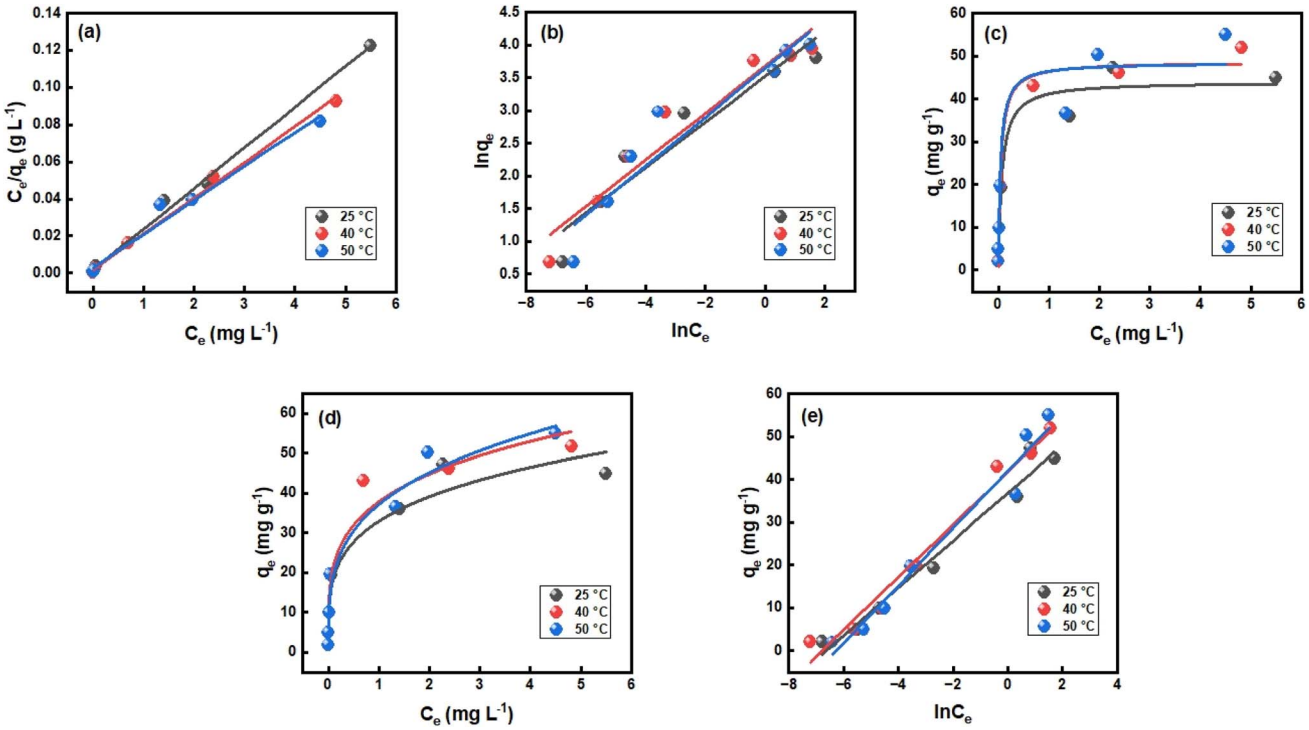

Fig. 6 (a) Linear Langmuir isotherm model, (b) linear Freundlich isotherm model, (c) non-linear Langmuir isotherm model, (d) non-linear Freundlich isotherm model and (e) Temkin isotherm model for TC (pH = 5, m-GO/Fe_3O_4/CMC = 0.1 g L^{-1}, t = 25 min, shaking speed = 250 rpm, temp. = 25, 40 and 50 °C respectively).

within the composite matrix.[59] The EDX spectral analysis are shown in Fig. 2(d) provided valuable insights into the elemental composition of m-GO/Fe_3O_4/CMC. The EDX analysis confirmed the presence of carbon (C) and oxygen (O), which were fundamental constituents of both GO and CMC, along with distinct signals for iron (Fe), indicating the successful incorporation of Fe_3O_4 nanoparticles into the composite. The elemental composition aligned well with the expected structure of m-GO/Fe_3O_4/CMC, suggesting effective anchoring of Fe_3O_4 onto the GO surface. The observed rough and heterogeneous surface morphology might have resulted from the interaction and partial aggregation of these nanoparticles on the GO sheets, which enhanced the textural complexity of the composite. Furthermore, the elevated oxygen content supported FTIR findings, reinforcing the presence of oxygenated functional groups within the composite. It should be noted that the detected copper (Cu) signal originated from the Cu grid used during SEM-EDX analysis and represented a background artifact rather than a component of the material.

Table 3 Different isotherm parameters of TC adsorption onto m-GO/Fe_3O_4/CMC

Isotherm models	Curve fitting	Parameters	25 °C	40 °C	50 °C
Langmuir	Linear	q_m (mg g^{-1})	45.5581	51.4933	54.7346
		k_L (L mg^{-1})	12.9872	13.0892	6.8998
		R^2	0.9952	0.9969	0.9809
	Non-linear	q_m (mg g^{-1})	44.0051	48.6490	48.4744
		k_L (L mg^{-1})	14.3928	20.4715	22.7237
		R^2	0.9569	0.9895	0.9425
Freunlich	Linear	K_F ($mg^{1-1/n}$ $L^{-1/n}$ g^{-1})	33.5572	39.6975	38.1927
		n	2.8998	2.8018	2.6881
		R^2	0.9280	0.9326	0.9005
	Non-linear	K_F ($mg^{1-1/n}$ $L^{-1/n}$ g^{-1})	32.9478	37.8684	37.1723
		n	4.0206	4.1114	3.5412
		R^2	0.9490	0.9464	0.9609
Temkin	Linear	K_T (L g^{-1})	756.9815	889.7684	531.0389
		b (J mol^{-1})	445.2921	422.6786	402.0913
		R^2	0.9722	0.9788	0.9669

Table 4 Comparison of the m-GO/Fe_3O_4/CMC adsorbent with other adsorbents

Antibiotic	Adsorbent	Adsorption capacity, q_m (mg g^{-1})	Time	Temperature (°C)	pH	Reference
Tetracycline	Amino-Fe(III) functionalized SBA15	65.98	24 h	25	4.5–5.6	91
	CA-H_2O_2	52	120 min	25	4	92
	Fe-doped zeolite	204	24 h	25	6	93
	Anaerobic granular sludge	4.62	13 h	45	3	94
	Illite	32	8 h	25	5–6	95
	Chitosan-olive pomace adsorbing films	16	1 h	27	8	96
	Electronic waste derived magnetic GO/Fe_3O_4/CMC nanocomposite	**54.73**	**25 min**	**50**	**5**	**This study**

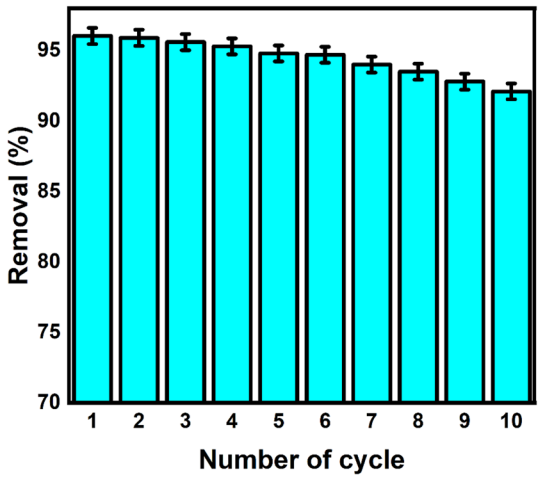

Fig. 7 Reusability and stability study test for the adsorbent m-GO/Fe_3O_4/CMC.

3.1.6. Transmission electron microscopy (TEM). The TEM images of GO and m-GO/Fe_3O_4/CMC are shown in Fig. 3(a and b). The TEM image in Fig. 3(a) showed that the synthesized GO exhibited a typical wrinkled and sheet-like structure.[60] This sheet-like morphology of GO was formed due to crumpling and scrolling, demonstrating its large surface area.[61] In Fig. 3(b), the TEM image of the m-GO/Fe_3O_4/CMC composite, taken at 100 nm, displayed a hybrid nanostructured porous network with a loose agglomeration, suggesting a high surface area. The contrast observed between the GO sheets and Fe_3O_4 nanoparticles confirmed the successful formation of the composite and the integration of inorganic and organic phases.[59] The visible clustering likely resulted from interactions between the CMC chains and the Fe_3O_4 surface, which facilitated network formation.[62]

3.2 Adsorption of TC by synthesized m-GO/Fe_3O_4/CMC nanoadsorbent

3.2.1. Effect of adsorbent dose. The adsorbent dosage plays an essential role in determining the availability of active sites for contaminant removal. A series of batch experiments were conducted by using various adsorbent doses at an initial TC concentration of 2 mg L^{-1}. The studies were performed with adsorbent doses of 1, 2, 3, 5, 7, and 10 mg. The effect of adsorbent dosage on TC adsorption by m-GO/Fe_3O_4/CMC is presented in Fig. 4(a). As shown in the figure, increasing the adsorbent dose led to higher TC removal efficiency. This improvement was attributed to the presence of CMC, which contained numerous functional groups that enhanced the availability of active sites for adsorption.[63] This, in turn, increased the adsorbent's surface area and provided additional binding sites, facilitating the binding of ions to the adsorption sites.[17,42] Beyond 2 mg, the adsorption trend exhibited near-linear behavior, indicating that most of the available adsorbate had already been adsorbed and adding more adsorbent did not significantly increase removal efficiency. This approach avoided unnecessary use of excess adsorbent, making the process both efficient and cost-effective. Based on the results, 2 mg for 20 mL (0.1 g L^{-1}) was identified as the optimal adsorbent dosage for subsequent experiments.

3.2.2. Effect of contact time. The impact of contact time on the adsorption of TC onto m-GO/Fe_3O_4/CMC nanocomposite was examined for 5 to 90 min. As shown in Fig. 4(b), the adsorption process occurred rapidly with increasing time, reaching maximum removal efficiency after 25 min, at which point the system reached equilibrium. Beyond this point, no noteworthy increase in adsorption percentage was observed. The initial rapid adsorption within the first 25 min could be clarified by the abundance of active sites on the m-GO/Fe_3O_4/CMC nanocomposite. With the progression of time, the remaining vacant adsorption sites became increasingly difficult to occupy, primarily due to repulsive interactions among solute molecules within the solid phase and the bulk solution.[64] The highest removal efficiency was credited to the multifunctional nature of m-GO/Fe_3O_4/CMC as an adsorbent, which facilitated adsorption through different mechanisms, including hydrogen bonding, electrostatic forces, and π–π interactions.[65] Based on these discoveries, an optimal contact time of 25 min (with a removal efficiency of 96.04%) was chosen for further investigations.

3.2.3. Effect of pH. The ionization state of surface functional groups on materials can be controlled by altering the solution conditions, which in turn influences their adsorption capacity.[66] The speciation of TC is also highly dependent on the solution pH, given its pK_a values of 3.3, 7.7, and 9.7.[67] To investigate the impact of solution pH on the adsorption performance of the m-GO/Fe_3O_4/CMC nanocomposite, adsorption experiments were conducted over a pH extend of 2.0 to

10.0. A fixed adsorbent dosage of 2 mg was utilized at a temperature of 25 °C, with an initial TC concentration of 2 mg L^{-1}.

As shown in Fig. 4(c), the adsorption performance of the m-GO/Fe_3O_4/CMC nanocomposite for removing TC significantly improved as the pH expanded from 2.0 to 5.0. However, when the pH rose from 6.0 to 10.0, the adsorption capacity exhibited a declining trend. TC can exist in three distinct forms depending on the pH: cationic at pH < 3.3, zwitterionic at pH 3.3–7.68, and anionic at pH > 7.68.[68] The influence of solution pH on adsorption capacity can be attributed to the electrostatic interactions between the charged surface of the nanocomposite and the different forms of TC. At pH below the point of zero charge (pH_{pzc} = 3.5), the low adsorption capacity was due to electrostatic repulsion between the cationic form of TC (TCH_3^+), and the positively charged surface of the nanocomposite. As the pH reached 5.0, TC transitioned to its zwitterionic form (TCH±), and the electrostatic attraction between the positively charged TC and the negatively charged surface of the nanocomposite became favorable, leading to enhanced adsorption capacity. Notably, the zwitterionic form reached its maximum concentration within the pH range of 5.0–6.0, resulting in the highest adsorption capacity for TC within this pH range. When the pH increased from 6.0 to 10.0, the formation of anionic TC species (TCH^- and TC^{2-}) caused electrostatic repulsion between these anions and the negatively charged surface of the nanocomposite, leading to a reduction in adsorption capacity.[67] Based on these discoveries, an initial pH of 5.0 was selected for subsequent adsorption experiments.

3.2.4. Effect of initial concentration. The effect of TC concentration on the adsorption performance of m-GO/Fe_3O_4/CMC was investigated by adjusting the initial TC concentration between 0.2 and 10 mg L^{-1} at a solution pH of 5, with an adsorbent dose of 2 mg and a temperature of 25 °C (Fig. 4(d)). As the initial TC concentration increased from 0.2 to 10 mg L^{-1}, the adsorption efficiency diminished from 99.43% to 44.99%. This decline in removal efficiency at higher TC concentrations could be credited to the limited availability of adsorption sites, saturation of the adsorbent's binding capacity, and increased competition among TC molecules for these sites.[17] The adsorption mechanism, driven by electrostatic forces, hydrogen bonding, and π–π interactions, became less effective as the adsorbent became saturated with TC molecules.[47] Based on the higher removal efficiency observed, 2 mg L^{-1} was identified as the optimal initial concentration of TC for further studies.

3.2.5. Kinetic studies of adsorption. Adsorption kinetics govern the rate at which adsorption occurs, providing insight into the time needed for the system to achieve equilibrium. To analyze the adsorption kinetics, experimental data were assessed utilizing Lagergren's pseudo-first-order, Ho's pseudo-second-order, Elovich, and Weber–Morris intraparticle diffusion models.

The Lagergren's pseudo-first-order model can be described by the following equation:[49,69]

$$\ln(q_e - q_t) = \ln q_e - k_1 t \quad (4)$$

Here, q_e represents the adsorbed amount at equilibrium (mg g^{-1}), q_t denotes the adsorbed amount at time t (mg g^{-1}), and k_1 is the rate constant at equilibrium (g mg^{-1} min^{-1}). By plotting $\ln(q_e - q_t)$ against t, the actual values of q_e and k_1 can be determined from the intercept and slope, respectively.

Ho's pseudo-second-order model can be investigated as follows:[46,70]

$$\frac{t}{q_t} = \frac{1}{k_2 {q_e}^2} + \frac{t}{q_e} \quad (5)$$

Here, k_2 represents the pseudo-second-order rate constant (g mg^{-1} min^{-1}). By plotting t/q_t against t, the actual values of q_e and k_2 can be determined from the slope and intercept, respectively.[71]

The Elovich kinetic model can be expressed using the following equation:[72]

$$q_t = \frac{1}{\beta}\ln(\alpha\beta) + \frac{1}{\beta}\ln t \quad (6)$$

Here, α represents the initial adsorption rate (mg g^{-1} min^{-1}), and β is the desorption constant. By plotting $\ln t$ *versus* q_t, the constants α and β can be determined from the intercept and slope of the plot, respectively.

The intraparticle diffusion model can be explained according to the following equation:[73]

$$q_t = k_i t^{0.5} + C_i \quad (7)$$

Here, q_t represents the amount of adsorbed TC at time t, k_i (mg g^{-1} $min^{-0.5}$) is the intraparticle diffusion rate constant, and C_i is a constant derived from the intercept of the equation. By plotting q_t against $t^{0.5}$, the values of k_i and C_i can be determined from the slope and intercept, respectively.

The non-linear forms of the pseudo-first-order and pseudo-second-order models are represented in eqn (8) and (9):[74]

$$q_t = q_e(1 - e^{(-k_1 t)}) \quad (8)$$

$$q_t = \frac{k_2 {q_e}^2 t}{1 + k_2 q_e t} \quad (9)$$

Here, q_t is the amount of adsorbate adsorbed at time t, q_e is the equilibrium adsorption capacity, k_1 is the rate constant for the pseudo-first-order model, and k_2 is the rate constant for the pseudo-second-order model.

For the linear pseudo-first-order, pseudo-second-order, non-linear pseudo-first-order, pseudo-second-order, Elovich, and intraparticle diffusion kinetic models, the experimental data are plotted in Fig. 5(a–e), respectively. The corresponding parameters, obtained from the intercept and slope of the plots, are summarized in Table 2.

The correlation coefficients (R^2) serve as a measure to evaluate the suitability of the kinetic models by assessing their fitting accuracy. As shown in Fig. 5(b), the linear pseudo-second-order kinetic model demonstrated a significantly high correlation coefficient (R^2 = 0.9999). This strong agreement between the experimental data and the linear curve fitting equation of the pseudo-second-order model highlighted its

effectiveness in characterizing the adsorption behavior and the rate at which TC was adsorbed onto the m-GO/Fe_3O_4/CMC adsorbent. These results suggested that the adsorption process was best described by linear pseudo-second-order kinetics, indicating that chemisorption was the dominant mechanism. In this process, the rate-limiting step likely involved chemical interactions between the adsorbate molecules and the adsorbent surface.[75]

3.2.6. Isotherm studies of adsorption. Adsorption isotherm models provide valuable information on the adsorption mechanism, the nature of active sites, and the adsorption capacity of an adsorbent. To analyze isotherms, experimental data were fitted to Langmuir, Freundlich, and Temkin isotherm models. Specifically, the Langmuir isotherm model is employed to determine the maximum adsorption capacity, suggesting that the adsorption process is homogeneous and involves the formation of a monolayer of adsorbate on the adsorbent's surface.[76] This model assumes no interactions between molecules at different sites and that the heat of adsorption is constant across all sites, independent of the number of occupied sites.[70,77] While the Freundlich model does not provide a measure of adsorption capacity, it is useful for understanding heterogeneous adsorption processes, indicating that the active sites on the adsorbent have varying energies.[78] On the other hand, the Temkin model helps elucidate the physical and chemical characteristics of the adsorption process.[79] The linearized forms of these models can be expressed by the following equations:[78–80]

Langmuir equation:

$$\frac{C_e}{q_e} = \frac{1}{K_L q_m} + \frac{C_e}{q_m} \quad (10)$$

Freundlich equation:

$$\ln q_e = \ln K_F + \frac{1}{n}\ln C_e \quad (11)$$

Temkin equation:

$$q_e = \frac{RT}{b}\ln K_T + \frac{RT}{b}\ln C_e \quad (12)$$

The non-linear expressions of the Langmuir isotherm and the Freundlich isotherm models are given by the following eqn (13) and (14), respectively:[81]

$$q_e = \frac{q_m K_L C_e}{1 + K_L C_e} \quad (13)$$

$$q_e = K_F (C_e)^{1/n} \quad (14)$$

where C_e is the equilibrium concentration of TC (mg L^{-1}), q_e represents the amount of TC adsorbed at equilibrium (mg g^{-1}), and q_m is the maximum adsorption capacity of m-GO/Fe_3O_4/CMC at monolayer coverage (mg g^{-1}). K_L is the dimensionless Langmuir adsorption constant, while K_F is the Freundlich adsorption constant ($mg^{1-1/n}\ L^{-1/n}\ g^{-1}$), with n being a constant related to adsorption intensity. R denotes the universal gas constant (J K^{-1} mol^{-1}), and T represents the absolute temperature (K). K_T is the equilibrium binding constant (L g^{-1}), and b is the Temkin constant associated with the heat of adsorption (J mol^{-1}).

For the Langmuir isotherm, Freundlich isotherm, and Temkin isotherm models, the experimental data are plotted in both linear and non-linear forms, as illustrated in Fig. 6(a–e). The relevant parameters, derived from the intercepts and slopes of these plots, are summarized in Table 3.

Based on the correlation coefficient (R^2) values obtained from fitting the experimental data to different isotherm models, the Langmuir linear model provided the best description of TC adsorption. The strong agreement between the adsorption data and the Langmuir linear isotherm indicated that the adsorption of TC onto m-GO/Fe_3O_4/CMC followed a monolayer adsorption mechanism, even on heterogeneous surface.[82] This implied that TC molecules formed a single layer on the adsorbent surface, while additional adsorption was mainly influenced by lateral interactions among the adsorbed molecules.[83] Additionally, the maximum adsorption capacity (q_m) was observed to increase with rising temperatures, suggesting that higher temperatures favored the adsorption process. This enhancement could be attributed to multiple factors: elevated temperatures improved the molecular mobility of TC, allowing more effective interactions with active adsorption sites on the m-GO/Fe_3O_4/CMC surface,[17,84] while the increased kinetic energy facilitated deeper diffusion of TC molecules into the adsorbent structure, thereby improving adsorption capacity.[85] From the Langmuir isotherm linear fitting, the maximum adsorption capacities (q_m) of m-GO/Fe_3O_4/CMC for TC were determined to be 45.56, 51.49, and 54.73 mg g^{-1} at 25, 40, and 50 °C, respectively.

3.2.7. Comparison of the m-GO/Fe_3O_4/CMC adsorbent with other adsorbents. The highest adsorption capacity of m-GO/Fe_3O_4/CMC has been compared to those of the other adsorbents reported in prior studies (Table 4). The results demonstrate that the synthesized nanocomposite exhibits a competitive adsorption capacity, despite the fact that some of the other adsorbents required more complex synthesis procedures. In this study, the equilibrium time was achieved in just 25 min, and the adsorbent dose was significantly low (0.1 g L^{-1}). Considering that waste Li-ion batteries are one of the most prevalent forms of electronic waste globally, they offer a promising source for deriving valuable materials for the removal of antibiotics from water. Additionally, the nanocomposite developed in this study provides the added benefit of easy separation through the application of an external magnetic field.

3.2.8. Reusability and stability study. The reusability of adsorbents is a key factor in assessing their practical and cost-effective application in wastewater treatment, making it a crucial environmental and economic consideration. After the adsorption of TC, the m-GO/Fe_3O_4/CMC nanoadsorbent was effectively separated using an external magnetic field and subsequently regenerated through methanol treatment.[17,47] Notably, this nanoadsorbent displayed remarkable reusability and recyclability, as illustrated in Fig. 7. The results demonstrated that the nanoadsorbent could be reused up to 10 cycles,

with only a minor reduction in removal efficiency from 96% to 92%. While some recent studies have achieved higher recycling cycles, they required substantially higher adsorbent dosages ($\gg 0.15$ g L^{-1}) and extended equilibrium times of several hours.[86,87] On the other hand, our study employed a much lower adsorbent dosage (0.1 g L^{-1}) and reached equilibrium within just 25 min. This highlights the superior efficiency and practicality of the m-GO/Fe_3O_4/CMC nanoadsorbent, achieving comparable or better performance with minimal adsorbent usage and significantly shorter processing duration. The exceptional reusability of the m-GO/Fe_3O_4/CMC nanoadsorbent highlights its potential as an efficient and environmentally friendly solution for TC removal from water sources. Its ability to be reused multiple times offers both economic and ecological benefits, reinforcing its viability for sustainable water treatment applications.

3.2.9. Adsorption mechanism. The m-GO/Fe_3O_4/CMC nanoadsorbent is enriched with plenteous carboxylic and oxygen-containing functional groups, upgrading its adsorption efficiency. The potential adsorption mechanism between TC and m-GO/Fe_3O_4/CMC basically includes π–π interactions, electrostatic forces and hydrogen bonding. FTIR characterization revealed an absorption band at 1454 cm^{-1}, corresponding to the aromatic C=C bonds within the nanoadsorbent. This proposed that the π electrons of the TC aromatic rings could interact with the aromatic structures of the nanoadsorbent *via* π–π interactions.[88] Furthermore, pH-dependent adsorption studies revealed that the adsorption was most favorable at solution pH levels that promoted electrostatic attraction between the charged TC molecules and the charged surface of the nanoadsorbent. Electrostatic interactions were identified as the dominant adsorption mechanism. However, TC removal was also observed at lower pH values, despite the presence of electrostatic repulsion, yet with lower adsorption efficiency.[89] Additionally, hydrogen bonding played a significant role in the adsorption process, as interactions involving nitrogen- and oxygen-containing functional groups contribute to the physicochemical properties of the system.[90]

4. Conclusion

A magnetically separable m-GO/Fe_3O_4/CMC nanoadsorbent was successfully synthesized from electronic waste for the efficient removal of TC from aqueous media. The synthesized nanoadsorbent was characterized utilizing various instrumental techniques, confirming the presence of highly dispersed nanoparticles on the GO surface and the superparamagnetic behavior of the nanocomposite, exhibiting a saturation magnetization of 50.69 emu g^{-1}. Adsorption studies revealed that the nanoadsorbent achieved a remarkable 96.04% TC removal within just 25 min at pH 5.0, using an adsorbent dose of 0.1 g L^{-1}. VSM analysis confirmed the magnetic properties of the m-GO/Fe_3O_4/CMC nanoadsorbent, enabling easy separation from the adsorption mixture using an external magnetic field. This convenient separation enhanced its reusability, making it an amazing candidate for repeated applications. Adsorption isotherm and kinetic studies indicated that TC adsorption onto the nanoadsorbent followed the Langmuir isotherm model, with a maximum adsorption capacity of 54.73 mg g^{-1}, and adjusted to the pseudo-second-order kinetic model. The adsorption mechanism was primarily driven by hydrogen bonding, π–π interactions, and electrostatic forces. Reusability tests demonstrated the nanoadsorbent's outstanding stability, maintaining high adsorption effectiveness indeed after ten cycles. These findings suggest that electronic waste-derived m-GO/Fe_3O_4/CMC nanoadsorbent is a promising material for the removal of residual TC antibiotics from waste water.

Conflicts of interest

The authors declare no conflict of interest.

Data availability

Data will be available on request.

Acknowledgements

The authors gratefully acknowledge the Bangladesh Council of Scientific and Industrial Research (BCSIR) for financial support (Research and Development, Ref. No: 39.02.0000.011.14.180.2024/1116, Date 14.01.2025) and for providing necessary facilities. SEM-EDX and VSM analyses were conducted at IERD and IGCRT, whereas XRD and FTIR analyses were supported by CARS. TEM analysis was successfully performed at BAEC, which is also sincerely appreciated.

References

1 B. P. Upoma, S. Yasmin, M. A. Ali Shaikh, T. Jahan, M. A. Haque, M. Moniruzzaman and M. H. Kabir, *ACS Omega*, 2022, **7**, 29655–29665.
2 V. Homem and L. Santos, *J. Environ. Manage.*, 2011, **92**, 2304–2347.
3 L.-T.-C. Dang, H.-V.-T. Phan, M.-T. Dao, T.-T. Dang, S. Suvokhiaw, N.-T. Do, T.-A.-M. Nguyen, V.-K. Nguyen and L.-T.-T.-T. Hoang, *RSC Adv.*, 2024, **14**, 34457–34470.
4 Y. Dai, M. Liu, J. Li, S. Yang, Y. Sun, Q. Sun, W. Wang, L. Lu, K. Zhang, J. Xu, W. Zheng, Z. Hu, Y. Yang, Y. Gao and Z. Liu, *Sep. Sci. Technol.*, 2020, **55**, 1005–1021.
5 L. Xu, H. Zhang, P. Xiong, Q. Zhu, C. Liao and G. Jiang, *Sci. Total Environ.*, 2021, **753**, 141975.
6 M. Beiranvand, S. Farhadi and A. Mohammadi-Gholami, *RSC Adv.*, 2022, **12**, 34438–34453.
7 Y. Zhao, F. Tong, X. Gu, C. Gu, X. Wang and Y. Zhang, *Sci. Total Environ.*, 2014, **470–471**, 19–25.
8 F. Ahmad, D. Zhu and J. Sun, *Environ. Sci. Eur.*, 2021, **33**, 64.
9 A. El Amri, L. Kadiri, R. Hsissou, A. Lebkiri, Z. Wardighi, E. H. Rifi and A. Lebkiri, *J. Mol. Struct.*, 2023, **1272**, 134098.
10 S.-F. Yang, C.-F. Lin, C.-J. Wu, K.-K. Ng, A. Yu-Chen Lin and P.-K. Andy Hong, *Water Res.*, 2012, **46**, 1301–1308.
11 X. Wang, J. Jing, M. Zhou and R. Dewil, *Chin. Chem. Lett.*, 2023, **34**, 107621.

12 B. Chen, Y. Meng, J. Sha, C. Zhong, W. Hu and N. Zhao, *Nanoscale*, 2018, **10**, 34–68.
13 G. Zeng, Z. He, T. Wan, T. Wang, Z. Yang, Y. Liu, Q. Lin, Y. Wang, A. Sengupta and S. Pu, *Sep. Purif. Technol.*, 2022, **292**, 121037.
14 T. Bhoyar, B. M. Abraham, A. Gupta, D. J. Kim, N. R. Manwar, K. S. Pasupuleti, D. Vidyasagar and S. S. Umare, *J. Mater. Chem. A*, 2024, **12**, 979–992.
15 H. Peng and J. Guo, *Environ. Chem. Lett.*, 2020, **18**, 2055–2068.
16 S. Akter, M. S. Islam, M. H. Kabir, M. A. A. Shaikh and M. A. Gafur, *Arab. J. Chem.*, 2022, **15**, 103900.
17 M. S. Hossain, M. H. Kabir, M. A. A. Shaikh, M. A. Haque and S. Yasmin, *RSC Adv.*, 2024, **14**, 1431–1444.
18 L. Kadiri, A. Ouass, R. Hsissou, Z. Safi, N. Wazzan, Y. Essaadaoui, I. Lebkiri, O. El Khattabi, E. Housseine Rifi and A. Lebkiri, *J. Mol. Liq.*, 2021, **343**, 116971.
19 M.-L. Cui, Z.-X. Lin, Q.-F. Xie, X.-Y. Zhang, B.-Q. Wang, M.-L. Huang and D.-P. Yang, *Food Chem.*, 2023, **412**, 135554.
20 J. Shim, M. Kumar, R. Goswami, P. Mazumder, B.-T. Oh and P. J. Shea, *J. Hazard. Mater.*, 2019, **364**, 419–428.
21 N. Roy, S. Yasmin, A. K. Mohiuddin and S. Jeon, *Appl. Surf. Sci. Adv.*, 2023, **18**, 100517.
22 S. Yasmin, N. Roy, M. H. Kabir and S. Jeon, *Appl. Surf. Sci. Adv.*, 2022, **9**, 100235.
23 S. Yasmin, M. H. Kabir, N. Roy and S. Jeon, *ECS Adv.*, 2023, **2**, 024504.
24 T. Meng, L. Wang, H. Jia, T. Gong, Y. Feng, R. Li, H. Wang and Y. Zhang, *J. Colloid Interface Sci.*, 2019, **536**, 424–430.
25 A. K. Mohiuddin, S. Yasmin and S. Jeon, *Sens. Actuators, A*, 2023, **355**, 114314.
26 S. Yasmin, S. Cho and S. Jeon, *Appl. Surf. Sci.*, 2018, **434**, 905–912.
27 S. Yasmin, M. H. Kabir, M. A. A. Shaikh and S. Jeon, *ECS J. Solid State Sci. Technol.*, 2023, **12**, 111004.
28 S. Yasmin, M. S. Ahmed and S. Jeon, Nitrogen-Doped Graphene Supported Cobalt Oxide Nanocomposite as High Performance Electrocatalyst for Oxygen Reduction Reaction, **https://www.ingentaconnect.com/contentone/asp/jnn/2017/00000017/00000006/art00046**, (accessed April 22, 2025).
29 S. Yasmin, Y. Joo and S. Jeon, *Appl. Surf. Sci.*, 2017, **406**, 226–234.
30 S. M. Badawy, *Environ. Prog. Sustainable Energy*, 2016, **35**, 1485–1491.
31 N. Roy, S. Yasmin and S. Jeon, *Microchem. J.*, 2020, **153**, 104501.
32 M. Humayun Kabir, M. Yeasin Pabel, N. Tasnim Bristy, M. Abdus Salam, M. Shahriar Bashar and S. Yasmin, *RSC Adv.*, 2024, **14**, 36073–36083.
33 M. Yeasin Pabel, M. Humayun Kabir, M. Sanwar Hossain, F. Mojumder, S. Datta, M. Shahriar Bashar and S. Yasmin, *Mater. Adv.*, 2025, **6**, 2243–2252.
34 M. Y. Pabel, M. H. Kabir and S. Yasmin, *J. Energy Storage*, 2025, **119**, 116314.
35 M. Yeasin Pabel, S. Yasmin, M. A. A. Shaikh and M. H. Kabir, *Sens. Actuators, A*, 2024, **366**, 115028.
36 S. Maleky, A. Asadipour, A. Nasiri, R. Luque and M. Faraji, *J. Polym. Environ.*, 2022, **30**, 3351–3367.
37 W. Gao, M. Majumder, L. B. Alemany, T. N. Narayanan, M. A. Ibarra, B. K. Pradhan and P. M. Ajayan, *ACS Appl. Mater. Interfaces*, 2011, **3**, 1821–1826.
38 S. Shankar and S. A. John, *Sens. Actuators, B*, 2015, **221**, 1202–1208.
39 D. Wang, L. Liu, X. Jiang, J. Yu and X. Chen, *Colloids Surf., A*, 2015, **466**, 166–173.
40 N. Rattanachueskul, A. Saning, S. Kaowphong, N. Chumha and L. Chuenchom, *Bioresour. Technol.*, 2017, **226**, 164–172.
41 M. A. Salam, R. M. El-Shishtawy and A. Y. Obaid, *J. Ind. Eng. Chem.*, 2014, **20**, 3559–3567.
42 M. G. Azam, M. H. Kabir, M. A. A. Shaikh, S. Ahmed, M. Mahmud and S. Yasmin, *J. Water Process Eng.*, 2022, **46**, 102597.
43 S. Yasmin, M. S. Ahmed and S. Jeon, *J. Electrochem. Soc.*, 2015, **162**, B363.
44 S. Yasmin, M. S. Ahmed, D. Park and S. Jeon, *J. Electrochem. Soc.*, 2016, **163**, B491.
45 S. Eslami, M. A. Ebrahimzadeh and P. Biparva, *RSC Adv.*, 2018, **8**, 26144–26155.
46 M. H. Kabir, M. S. Hossain, M. M. Rahman, M. Ashrafuzzaman, M. Hasan, M. Y. Pabel, D. Islam, M. Shahriar Bashar, T. Faruque and S. Yasmin, *ACS Sustainable Resour. Manage.*, 2024, **1**, 1812–1823.
47 F. Mojumder, S. Yasmin, M. A. A. Shaikh, P. Chowdhury and M. H. Kabir, *J. Hazard. Mater. Adv.*, 2024, **14**, 100429.
48 X. Li, L. Ai and J. Jiang, *Chem. Eng. J.*, 2016, **288**, 789–797.
49 M. H. Kabir, M. J. Miah, A. K. Mohiuddin, M. S. Hossain, B. P. Upoma, M. A. A. Shaikh, M. Y. Pabel, F. Mojumder, R. Mahmud, N. I. Tanvir and S. Yasmin, *ACS Sustainable Resour. Manage.*, 2025, **2**, 256–266.
50 A. Zaman, J. T. Orasugh, P. Banerjee, S. Dutta, M. S. Ali, D. Das, A. Bhattacharya and D. Chattopadhyay, *Carbohydr. Polym.*, 2020, **246**, 116661.
51 H.-L. Guo, X.-F. Wang, Q.-Y. Qian, F.-B. Wang and X.-H. Xia, *ACS Nano*, 2009, **3**, 2653–2659.
52 R. Md Salim, J. Asik and M. S. Sarjadi, *Wood Sci. Technol.*, 2021, **55**, 295–313.
53 A. Dang, X. liu, Y. Wang, Y. Liu, T. Cheng, A. Zada, F. Ye, W. Deng, Y. Sun, T. Zhao and T. Li, *J. Hazard. Mater.*, 2023, **457**, 131846.
54 M. S. Raghu, K. Yogesh Kumar, M. K. Prashanth, B. P. Prasanna, R. Vinuth and C. B. Pradeep Kumar, *J. Water Process Eng.*, 2017, **17**, 22–31.
55 M. S. Hossain, S. Yasmin and M. H. Kabir, *J. Saudi Chem. Soc.*, 2024, **28**, 101873.
56 L.-T.-T.-T. Hoang, H.-V.-T. Phan, P.-N. Nguyen, T.-T. Dang, T.-N. Tran, D.-T. Vo, V.-K. Nguyen and M.-T. Dao, *Arch. Environ. Contam. Toxicol.*, 2024, **86**, 48–57.
57 M. G. Azam, M. H. Kabir, M. A. A. Shaikh, S. Ahmed, M. Mahmud and S. Yasmin, *J. Water Process Eng.*, 2022, **46**, 102597.
58 A. G. de Souza, R. F. S. Barbosa and D. S. Rosa, *J. Polym. Environ.*, 2020, **28**, 1851–1868.

59 E. A. Neskoromnaya, A. V. Melezhyk, E. S. Mkrtchan, A. E. Memetova and A. V. Babkin, *Inorg. Mater. Appl. Res.*, 2023, **14**, 358–367.
60 M. S. Amir Faiz, C. A. Che Azurahanim, S. A. Raba'ah and M. Z. Ruzniza, *Results Phys.*, 2020, **16**, 102954.
61 J. Keloth Paduvilan, P. Velayudhan, A. Amanulla, H. Joseph Maria, A. Saiter-Fourcin and S. Thomas, *Nanomaterials*, 2021, **11**, 1098.
62 C. Xiang, C. Wang, R. Guo, J. Lan, S. Lin, S. Jiang, X. Lai, Y. Zhang and H. Xiao, *J. Mater. Sci.*, 2019, **54**, 1872–1883.
63 M. Tanzifi, M. Tavakkoli Yaraki, Z. Beiramzadeh, L. Heidarpoor Saremi, M. Najafifard, H. Moradi, M. Mansouri, M. Karami and H. Bazgir, *Chemosphere*, 2020, **255**, 127052.
64 M. Esmaeili Bidhendi, Z. Poursorkh, H. Sereshti, H. Rashidi Nodeh, S. Rezania and M. Afzal Kamboh, *Int. J. Environ. Res. Publ. Health*, 2020, **17**, 4223.
65 D. Qiao, Z. Li, J. Duan and X. He, *Chem. Eng. J.*, 2020, **400**, 125952.
66 V. S. Munagapati, H.-Y. Wen, Y. Vijaya, J.-C. Wen, J.-H. Wen, Z. Tian, G. M. Reddy and J. R. Garcia, *Int. J. Phytoremediation*, 2021, **23**, 911–923.
67 J. L. Colaizzi and P. R. Klink, *J. Pharm. Sci.*, 1969, **58**, 1184–1189.
68 Y. Zhang, Z. Jiao, Y. Hu, S. Lv, H. Fan, Y. Zeng, J. Hu and M. Wang, *Environ. Sci. Pollut. Res.*, 2017, **24**, 2987–2995.
69 S. Nethaji, A. Sivasamy and A. B. Mandal, *Int. J. Sci. Environ. Technol.*, 2013, **10**, 231–242.
70 A. F. Hassan, A. M. Abdel-Mohsen and M. M. G. Fouda, *Carbohydr. Polym.*, 2014, **102**, 192–198.
71 A. M. Omer, G. S. Elgarhy, G. M. El-Subruiti, R. E. Khalifa and A. S. Eltaweil, *Int. J. Biol. Macromol.*, 2020, **148**, 1072–1083.
72 Adsorption-Membrane Hybrid Approach for the Removal of Azithromycin from Water: An Attempt to Minimize Drug Resistance Problem, **https://www.mdpi.com/2073-4441/13/14/1969**, (accessed March 20, 2025).
73 J. L. Marco-Brown, L. Guz, M. S. Olivelli, B. Schampera, R. M. Torres Sánchez, G. Curutchet and R. Candal, *Chem. Eng. J.*, 2018, **333**, 495–504.
74 M. Laxmi Deepak Bhatlu, P. S. Athira, N. Jayan, D. Barik and M. S. Dennison, *Adsorpt. Sci. Technol.*, 2023, **2023**, 7369027.
75 H. Shayesteh, R. Nodehi and A. Rahbar-Kelishami, *Surf. Interfaces*, 2020, **20**, 100615.
76 Efficient removal of pharmaceutical contaminants from water and wastewater using immobilized laccase on activated carbon derived from pomegranate peels | Scientific Reports, **https://www.nature.com/articles/s41598-023-38821-3**, (accessed March 21, 2025).
77 X. Zhang, Y. Li, M. Li, H. Zheng, Q. Du, H. Li, Y. Wang, D. Wang, C. Wang, K. Sui, H. Li and Y. Xia, *J. Colloid Interface Sci.*, 2019, **556**, 249–257.
78 T. Luo, X. Hou, Q. Liang, G. Zhang, F. Chen, Y. Xia, Q. Ru, L. Yao and Y. Wu, *J. Alloys Compd.*, 2018, **763**, 771–780.
79 A. Zahir, Z. Aslam, M. S. Kamal, W. Ahmad, A. Abbas and R. A. Shawabkeh, *J. Mol. Liq.*, 2017, **244**, 211–218.
80 D. G. Kinniburgh, *Environ. Sci. Technol.*, 1986, **20**, 895–904.
81 J. Wang, H. Huang, M. Wang, L. Yao, W. Qiao, D. Long and L. Ling, *Ind. Eng. Chem. Res.*, 2015, **54**, 5319–5327.
82 H. Shayesteh, F. Raji and A. R. Kelishami, *Surf. Interfaces*, 2021, **22**, 100806.
83 K. Fytianos, E. Voudrias and E. Kokkalis, *Chemosphere*, 2000, **40**, 3–6.
84 M. Ghaedi, K. Mortazavi, M. Montazerozohori, A. Shokrollahi and M. Soylak, *Mater. Sci. Eng., C*, 2013, **33**, 2338–2344.
85 S. Sahoo, Uma, S. Banerjee and Y. C. Sharma, *Desalin. Water Treat.*, 2014, **52**, 6703–6711.
86 J. Tang, L. Zong, B. Mu, Y. Kang and A. Wang, *Korean J. Chem. Eng.*, 2018, **35**, 1650–1661.
87 A. Pardo, H. Garcia, P. Ramirez, M. A. Carrillo-Alvarado, K. S. Krishna, N. Dominguez, M. T. Islam, H. Wang and J. C. Noveron, *Environ. Technol. Innovation*, 2018, **11**, 321–327.
88 A. Chowdhury, S. Kumari, A. A. Khan, M. R. Chandra and S. Hussain, *Colloids Surf., A*, 2021, **611**, 125868.
89 R. Rehman and S. Majeed, *Int. J. Phytoremediation*, 2022, **24**, 1004–1013.
90 M. K. Uddin, A. Malek, N. Nurul, A. H. Jawad and S. Sabar, *Int. J. Phytoremediation*, 2023, **25**, 393–402.
91 Z. Zhang, H. Lan, H. Liu and J. Qu, *Colloids Surf., A*, 2015, **471**, 133–138.
92 L. R. d. C. Costa and L. A. Féris, *J. Environ. Sci. Health, Part A: Toxic/Hazard. Subst. Environ. Eng.*, 2020, **55**, 1604–1614.
93 M. H. Jannat Abadi, S. M. M. Nouri, R. Zhiani, H. D. Heydarzadeh and A. Motavalizadehkakhky, *Int. J. Ind. Chem.*, 2019, **10**, 291–300.
94 K. Li, F. Ji, Y. Liu, Z. Tong, X. Zhan and Z. Hu, *Water Sci. Technol.*, 2013, **67**, 1490–1496.
95 P.-H. Chang, Z. Li, J.-S. Jean, W.-T. Jiang, C.-J. Wang and K.-H. Lin, *Appl. Clay Sci.*, 2012, **67–68**, 158–163.
96 V. Rizzi, D. Lacalamita, J. Gubitosa, P. Fini, A. Petrella, R. Romita, A. Agostiano, J. A. Gabaldón, M. I. Fortea Gorbe, T. Gómez-Morte and P. Cosma, *Sci. Total Environ.*, 2019, **693**, 133620.